

## PAPER

[View Article Online](#)  
[View Journal](#) | [View Issue](#)Cite this: *Mater. Adv.*, 2021,  
2, 4323Received 15th April 2021,  
Accepted 11th May 2021

DOI: 10.1039/d1ma00344e

[rsc.li/materials-advances](http://rsc.li/materials-advances)Remarkable synergy of borate and interfacial hole transporter on BiVO<sub>4</sub> photoanodes for photoelectrochemical water oxidation†Qijun Meng,<sup>a</sup> Biaobiao Zhang,<sup>b</sup> Hao Yang,<sup>a</sup> Chang Liu,<sup>d</sup> Yingzheng Li,<sup>d</sup> Alexander Kravchenko,<sup>a</sup> Xia Sheng,<sup>a</sup> Lizhou Fan,<sup>a</sup> Fusheng Li<sup>d</sup> and Licheng Sun<sup>a</sup>

Bismuth vanadate (BiVO<sub>4</sub>) is one of the most fascinating building blocks for the design and assembly of highly efficient artificial photosynthesis devices for solar water splitting. Our recent report has shown that borate treated BiVO<sub>4</sub> (B-BiVO<sub>4</sub>) results in an improved water oxidation performance. In this study, further improvement of both the photoelectrochemical (PEC) activity and stability of B-BiVO<sub>4</sub> was successfully achieved by introducing NiFeV LDHs as an oxygen evolution catalyst and interfacial hole transporter. Benefiting from the synergistic effect of co-catalyst and borate pretreatment, the as-prepared NiFeV/B-BiVO<sub>4</sub> exhibited a high photocurrent density of 4.6 mA cm<sup>-2</sup> at 1.23 V<sub>RHE</sub> and an outstanding onset potential of ~0.2 V<sub>RHE</sub> with good long-term stability. More importantly, NiFeV was found to play a pivotal role in the critically efficient suppression of charge combination on the BiVO<sub>4</sub> surface and acceleration of charge transfer rather than a mere electrocatalyst for water oxidation.

## 1. Introduction

Photoelectrochemical (PEC) water splitting is a promising way to produce hydrogen as a clean and renewable energy carrier using light-absorbing semiconductors.<sup>1–4</sup> Since the photocatalytic water oxidation activity of monoclinic bismuth vanadate (BiVO<sub>4</sub>) was discovered by Kudo *et al.* in 1998,<sup>5</sup> BiVO<sub>4</sub> has drawn tremendous attention in the domain of PEC water splitting by virtue of favorable band positions and a suitable bandgap of 2.4–2.5 eV, which can allow the absorption of 11% visible light spectrum.<sup>6–8</sup> Theoretically, the maximum photocurrent density and the solar-to-hydrogen conversion efficiency can reach values as high as 7.5 mA cm<sup>-2</sup> and 9% under AM 1.5G illumination, respectively.<sup>9</sup> Unfortunately, a pure BiVO<sub>4</sub> photoelectrode still suffers from excessive electron–hole recombination (a carrier mobility of ~4 × 10<sup>-2</sup> cm<sup>2</sup> V<sup>-1</sup> s<sup>-1</sup>), poor charge transport

properties (a hole diffusion length of ~70 nm), and sluggish water oxidation kinetics, mostly resulting in disappointing photocurrent densities.<sup>10</sup>

To alleviate these limitations, numerous approaches have been proposed that usually combine effective synthesis methods with multiple modification strategies, including crystal facet engineering,<sup>11–13</sup> construction of heterojunctions,<sup>14–16</sup> substitutional doping,<sup>17–19</sup> oxygen evolution catalyst (OEC) loading,<sup>20–24</sup> post-synthetic treatments,<sup>25–28</sup> *etc.* For example, a landmark work reported by Choi and co-workers displayed a nanoporous BiVO<sub>4</sub> film photoanode (mean particle size ~76 nm) *via* a two-step method of electrodeposition of BiOI and ensuing thermal conversion of BiOI to BiVO<sub>4</sub> by introducing a proper vanadium source.<sup>6,29</sup> The resulting BiVO<sub>4</sub> exhibited a high charge separation efficiency in the bulk ( $\eta_{\text{bulk}}$ ) up to 90% without routine doping or heterojunction, and after assembling a NiOOH/FeOOH OEC, a remarkable photocurrent density of 4.5 mA cm<sup>-2</sup> at 1.23 V *versus* reversible hydrogen electrode (RHE) was obtained under AM 1.5G illumination.<sup>6</sup> Inspired by the natural photosystem II (PSII), Li and co-workers successfully demonstrated a CoPO<sub>3</sub>/pGO/LDH/BiVO<sub>4</sub> composite photoanode,<sup>30</sup> where BiVO<sub>4</sub>, NiFe layered double hydroxide (LDH), partially oxidized graphene (pGO) and cobalt cubane molecular catalyst served as a light harvester, a hole storage layer, a charge transfer layer and an OEC, respectively. The composite photoanode possessed a remarkable photocurrent density of 4.45 mA cm<sup>-2</sup> with an ultralow onset potential of 0.17 V and superior stability. By combining p–n heterojunction engineering,

<sup>a</sup> Department of Chemistry, KTH Royal Institute of Technology, 10044 Stockholm, Sweden<sup>b</sup> Center of Artificial Photosynthesis for Solar Fuels, School of Science, Westlake University, 310024 Hangzhou, China<sup>c</sup> Institute of Natural Sciences, Westlake Institute for Advanced Study, Hangzhou, 310024 Zhejiang, China<sup>d</sup> State Key Laboratory of Fine Chemicals, Institute of Artificial Photosynthesis, DUT-KTH Joint Education and Research Center on Molecular Devices, Dalian University of Technology (DUT), 116024 Dalian, China

† Electronic supplementary information (ESI) available: SEM, EDS, XRD, and UV-vis absorption spectra, XPS, Mott–Schottky, and KIE results. See DOI: 10.1039/d1ma00344e

work function adjustment and co-catalyst loading,<sup>31</sup> Yang and co-workers designed and fabricated a NiFeO<sub>x</sub>/B-C<sub>3</sub>N<sub>4</sub>/Mo-BiVO<sub>4</sub> photoanode, achieving a photocurrent density of 5.93 mA cm<sup>-2</sup> at 1.23 V<sub>RHE</sub> (92% IPCE) with an astonishing applied bias photon-to-current efficiency (ABPE) of 2.67% at 0.54 V<sub>RHE</sub>. In a very recent review,<sup>32</sup> Lee and co-workers clearly elucidated the efficacy of established modification techniques on a BiVO<sub>4</sub> photoanode by applying post-synthetic N<sub>2</sub> treatment, Mo doping, an electron transfer layer of SnO<sub>2</sub>, and deposition of the NiFeO<sub>x</sub> electrocatalyst. The obtained NiFeO<sub>x</sub>/N, 1% Mo:BiVO<sub>4</sub>/SnO<sub>2</sub> photoanode also exhibited outstanding PEC performance with 5.8 mA cm<sup>-2</sup> and a maximum ABPE of 2.7%. It should be pointed out that loading with OECs contributed the most to the dramatic enhancement compared to other modifications,<sup>32</sup> aiming at promoting the surface charge transfer at the semiconductor/electrolyte interface ( $\eta_{\text{surface}}$ ) as well as long-term photostability.

On the one hand, these recently flourished modification strategies have elevated BiVO<sub>4</sub> to an unprecedented position as the most up-and-coming photoanode material. On the other hand, each of them developed thus far is often found to have limited efficacy in targeting an all-round improvement toward all aspects of charge carrier kinetics, catalytic kinetics of water oxidation, and even light absorption, in terms of PEC performance and fundamental understanding of the material and working principles.<sup>33,34</sup> The elaborately modified BiVO<sub>4</sub>-based PEC devices are therefore in growing appeal toward practical applications.<sup>2</sup>

In our previous work, a facile borate modification of a BiVO<sub>4</sub> photoanode (B-BiVO<sub>4</sub>) was reported, delivering an impressive enhancement in PEC performance with a photocurrent density of ~3.5 mA cm<sup>-2</sup> at 1.23 V<sub>RHE</sub> without any doping or OEC decoration.<sup>35</sup> An analogous phenomenon engendered by borate species was also presented in several reports.<sup>36–39</sup> However, the B-BiVO<sub>4</sub> photoanode gradually lost its superior PEC performance within 1 h due to the photocorrosion of the adsorbed borate groups by surface charge accumulation. In this study, we solved this problem *via* the integration of a NiFe-based LDH, an excellent electrocatalyst for oxygen evolution reaction (OER),<sup>40–42</sup> also recognized as the hole transfer and storage layer for photoelectrodes.<sup>30,43–45</sup> Under the synergetic effect of molecular borate and NiFeV co-modifications, the resulting NiFeV/B-BiVO<sub>4</sub> photoanode exhibited an outstanding photocurrent density of 4.6 mA cm<sup>-2</sup> at 1.23 V<sub>RHE</sub> with an ultra-low onset potential of ~0.2 V<sub>RHE</sub> and superior photostability. NiFeV OECs served as not only a sole electrocatalyst for water oxidation but also a hole reservoir that efficiently suppressed surface charge recombination and accelerated interfacial charge transfer. The results illustrated in this work provided a simple yet efficient strategy for the design of high-performance and stable planar photoanodes for PEC water splitting.

## 2. Experimental section

### 2.1 Materials

Fluorine-doped tin oxide (FTO) coated glass substrates were purchased from Pilkington (~8  $\Omega$  cm<sup>-2</sup>) and were successively

cleaned using Milli-Q water, ethanol and acetone. Bismuth nitrate pentahydrate (Bi(NO<sub>3</sub>)<sub>3</sub>·5H<sub>2</sub>O, 98%), vanadyl acetylacetonate (VO(acac)<sub>2</sub>, 98%), nitric acid solution (HNO<sub>3</sub>, 70%), *p*-benzoquinone (98%), potassium iodide (KI, 99%), vanadium chloride (VCl<sub>3</sub>, 97%), nickel chloride hexahydrate (NiCl<sub>2</sub>·6H<sub>2</sub>O, 98%), iron chloride hexahydrate (FeCl<sub>3</sub>·6H<sub>2</sub>O, 97%), boric acid (H<sub>3</sub>BO<sub>3</sub>, 99.5%), sodium sulfite (Na<sub>2</sub>SO<sub>3</sub>, 98%), sodium hydroxide (NaOH, 98%), potassium hydroxide (KOH, 85%), Nafion<sup>TM</sup> 117 containing solution (5%), borax anhydrous (Na<sub>2</sub>B<sub>4</sub>O<sub>7</sub>, 98%), and deuterium oxide (D<sub>2</sub>O, 99.9%) were purchased from Sigma-Aldrich and used as received. All organic solvents including 2-propanol ethanol, absolute ethanol, and dimethyl sulfoxide (DMSO) were of analytical reagent grade and used without further purification. Ultra-pure water (18.2 M $\Omega$  cm<sup>-1</sup>) supplied by a Milli-Q system (Merck Millipore) was used in all experiments.

### 2.2 Fabrication of BiVO<sub>4</sub> and B-BiVO<sub>4</sub>

The detailed fabrication processes of BiVO<sub>4</sub> and B-BiVO<sub>4</sub> photoanodes were essentially repeated according to our previous report and an established procedure from Choi's group.<sup>6,35</sup> In brief, 0.04 M Bi(NO<sub>3</sub>)<sub>3</sub> and 0.4 M KI were successively added into 50 mL HNO<sub>3</sub> aqueous solution (pH 1.7) with mild stirring for 15 min. Afterwards, 20 mL of EtOH containing 0.23 M *p*-benzoquinone was mixed into the above solution with constant stirring. The electrodeposition of the BiOI precursor was carried out using a standard three-electrode cell where an FTO substrate, a saturated Ag/AgCl electrode, and a platinum wire electrode (1 × 1 cm<sup>2</sup>) were used as the working electrode (WE), the reference electrode (RE), and the counter electrode (CE), respectively. The electrodeposition of BiOI precursor was carried out potentiostatically at -0.1 V<sub>Ag/AgCl</sub> for 3 min at room temperature. The BiOI film was converted to BiVO<sub>4</sub> by thermal treatment in air at 450 °C for 2 h (ramping rate: 2 °C min<sup>-1</sup>) after covering the BiOI film with 80  $\mu$ L of a DMSO solution containing 0.2 M VO(acac)<sub>2</sub>. After annealing, the electrodes were soaked in 1 M NaOH solution for 30 min on a lab shaker to remove excess V<sub>2</sub>O<sub>5</sub> from the surface of BiVO<sub>4</sub>. The final bare BiVO<sub>4</sub> electrodes were washed thoroughly with Milli-Q water and gently dried with air stream. A 1.0 M potassium borate (KBi) buffer solution (pH = 9.3 ± 0.1, 1.0 M H<sub>3</sub>BO<sub>3</sub> adjusted by KOH) was used for both the preparation of B-BiVO<sub>4</sub> and the ensuing photoelectrochemical measurements.

For the preparation of B-BiVO<sub>4</sub>, a bare BiVO<sub>4</sub> photoanode was immersed into the above borate buffer in a capped brown vial and then heated at 100 °C for 30 min in an oil bath to shorten the treatment time. After cooling, the B-BiVO<sub>4</sub> anode was taken out from the solution, rinsed with Milli-Q water and dried with gentle air stream.

### 2.3 Synthesis of layered double hydroxides (LDHs) (NiFeV, NiV and NiFe)

The LDH nanoparticles were synthesized according to a report from our group *via* a one-step hydrothermal method.<sup>46</sup> The mole ratios of each element in NiFeV (3 : 0.2 : 1), NiV (3 : 1) and NiFe (3 : 1) were tuned by mixing the corresponding NiCl<sub>2</sub>, FeCl<sub>3</sub> and VCl<sub>3</sub> in 80 mL H<sub>2</sub>O while keeping the total amount of metal



ions at 3.2 mmol. The suspension of NiV LDH in a mixed solvent of H<sub>2</sub>O, 2-propanol and Nafion (4 : 1 : 0.04) with a concentration of 0.5 mg mL<sup>-1</sup> was prepared for further co-catalyst loading onto BiVO<sub>4</sub>.

## 2.4 Fabrication of LDH/BiVO<sub>4</sub> and LDH/B-BiVO<sub>4</sub>

Prior to co-catalyst loading, the above LDH nanoparticle suspension (0.5 mg mL<sup>-1</sup>) was ultrasonicated for 2 h. 5 µL of the resulting uniform suspension was then directly drop-casted onto BiVO<sub>4</sub> or BiVO<sub>4</sub> electrodes with an active area of 0.5 × 0.5 cm<sup>2</sup> and was allowed to dry by evaporation under ambient conditions. In addition to LDH/B-BiVO<sub>4</sub> electrodes, LDH/BiVO<sub>4</sub> electrodes were also prepared for comparison using the same methods described earlier.

## 2.5 Material characterization

The surface morphology and composition of LDH nanoparticles and the ensuing BiVO<sub>4</sub>-based photoelectrodes were determined using a field emission scanning electron microscope (FE-SEM, Hitachi, Regulus 8230) equipped with an energy-dispersive X-ray spectroscopy (EDX) detector (Oxford Ultim EXTREME). Transmission electron microscopy (TEM, JEOL JEM2100F) and high-resolution TEM (HRTEM) images were recorded at an acceleration voltage of 200 kV. The crystal structures of the samples were characterized by powder X-ray diffraction (PXRD, D8 Advance Bruker with Cu Kα (λ = 1.5406 Å) radiation. The surface chemical states and composition of the films were characterized by X-ray photoelectron spectroscopy (XPS) (ESCALAB Xi+, Thermo Fisher, UK) with a monochromated Al Kα radiation source (1486.6 eV). All binding energies were calibrated for specimen charging by referencing the C 1s peak to 284.8 eV. The optical absorption of BiVO<sub>4</sub> photoanodes was tested using an UV-vis diffuse reflectance (UV3600, Shimadzu, Japan) spectrophotometer in the range of 300–800 nm.

## 2.6 Photoelectrochemical measurements

All photoelectrochemical tests were performed using a CHI 660E potentiostat at room temperature in the same three-electrode configuration, except the use of the BiVO<sub>4</sub> photoanode as the WE. A NEWPORT LCS-100 solar simulator (type 94011A-ES, a 100 W Xenon arc lamp with an AM 1.5G filter) was used as the illumination source. 1.0 M Potassium borate buffer solution (pH 9.3) was used as the electrolyte for all PEC measurements. For all cases, light is irradiated from the back side of the FTO substrate and the illuminated areas were fixed at 0.5 × 0.5 cm<sup>2</sup>. For sulfite oxidation, 0.2 M Na<sub>2</sub>SO<sub>3</sub> was added into the electrolyte as a hole scavenger. *J*-*V* curves both under AM1.5 illumination and in the dark were obtained by linear sweep voltammetry (LSV) with a scan rate of 10 mV s<sup>-1</sup>. Electrochemical impedance spectroscopy (EIS) spectra of the electrodes were measured at 0.6 V<sub>RHE</sub> at frequencies ranging from 100 kHz to 0.01 Hz. Mott-Schottky (MS) spectra were obtained in the voltage window of 0–0.4 V<sub>RHE</sub> in the dark with a 10 mV increment and 1 kHz frequency. The incident photon-to-current conversion efficiency (IPCE) was measured at 1.23 V<sub>RHE</sub> using a Zahner CIMP-QE/IPCE system. Intensity modulated photocurrent spectroscopy

(IMPS) was performed on Zahner IMPS electrochemical workstation setup with the scanning frequency in the range of 0.1 Hz to 10 kHz (amplitude: 5 mV).<sup>20,47</sup> The modulated light source (10 mW cm<sup>-2</sup>) for IMPS characterization was a calibrated light-emitting diode (LED). H/D kinetic isotope effect (KIE) measurements were performed according to a previous report<sup>20</sup> by comparing photocurrent densities at different overpotentials (η) in 0.1 M anhydrous borax (Na<sub>2</sub>B<sub>4</sub>O<sub>7</sub>) H<sub>2</sub>O and D<sub>2</sub>O solutions, with pH values of 9.303 and 9.445 (measured using a 781 pH/Ion Meter, Metrohm), respectively. The long-term electrolysis was carried out with a constant potential at 0.6 V<sub>RHE</sub>. The actual amount of oxygen evolution was determined by gas chromatography (GC-2014 SHIMADZU). The amount of O<sub>2</sub> produced was calculated theoretically by converting the charge passed to µmol gas according to Faraday's law.

## 2.7 Relative equations

The recorded potential *versus* Ag/AgCl (*E*<sub>Ag/AgCl</sub>) was converted against reversible hydrogen electrode (RHE) according to the Nernst equation:

$$E_{\text{RHE}} = E_{\text{Ag/AgCl}} + 0.197 + 0.059 \times \text{pH} \quad (1)$$

The applied bias photon-current efficiency (ABPE) was calculated from the LSV curves of BiVO<sub>4</sub> photoanodes:

$$\text{ABPE} (\%) = \frac{(J_{\text{light}} - J_{\text{dark}}) \times (1.23 - V_{\text{RHE}})}{P_{\text{light}}} \times 100\% \quad (2)$$

The light harvesting efficiency (LHE) of the BiVO<sub>4</sub> photoanode was calculated from the UV-Vis diffuse reflectance spectra:

$$\text{LHE} (\%) = (1 - 10^{-A}) \times 100\% \quad (3)$$

where *A* is the light absorbance measured by UV-vis spectroscopy.

The photocurrent density arising from PEC performance (*J*<sub>PEC</sub>) can be described as follows:

$$J_{\text{PEC}} = J_{\text{abs}} \times \eta_{\text{bulk}} \times \eta_{\text{surface}} \quad (4)$$

$$J_{\text{abs}} (\text{mA cm}^{-2}) = e \times \int_{300 \text{ nm}}^{\lambda_{\text{abs}}} \text{LHE} \frac{f(\lambda)}{h\nu} d\lambda \quad (5)$$

where *J*<sub>abs</sub> is the photocurrent density at 100% internal quantum efficiency, which is obtained by integrating the distribution of solar power density *f*(λ) with light absorption LHE of the photoanode;<sup>48,49</sup> *e* is the elementary charge (1.602 × 10<sup>-19</sup> C); η<sub>bulk</sub> is the yield of the photogenerated holes from the bulk that reaches the electrode/electrolyte interface, while η<sub>surface</sub> is the charge injection efficiency of those surface-reaching holes into the electrolyte for ensuing water oxidation.

$$\eta_{\text{bulk}} (\%) = \frac{J_{\text{sulfite}}}{J_{\text{abs}}} \times 100\% \quad (6)$$

$$\eta_{\text{surface}} (\%) = \frac{J_{\text{water}}}{J_{\text{sulfite}}} \times 100\% \quad (7)$$

where *J*<sub>water</sub> and *J*<sub>sulfite</sub> are the photocurrent densities for PEC water oxidation and sulfite oxidation, respectively.





The H/D KIE values can be defined as

$$\text{KIE}_{\text{H/D}} = \left[ \frac{k_{\text{H}}}{k_{\text{D}}} \right]_{\eta} = \left[ \frac{J_{\text{H}}}{J_{\text{D}}} \right]_{\eta} \times 100\% \quad (8)$$

where  $k_{\text{H}}$  and  $k_{\text{D}}$  are the rate constants and  $J_{\text{H}}$  and  $J_{\text{D}}$  are the photocurrent densities measured in 0.1 M  $\text{Na}_2\text{B}_4\text{O}_7 \cdot \text{H}_2\text{O}$  and  $\text{D}_2\text{O}$  solutions, respectively. The pD value was calculated by adding 0.4 to the value of the pH meter reading. The overpotentials ( $\eta$ ) in  $\text{H}_2\text{O}$  and  $\text{D}_2\text{O}$  solutions were corrected as reported in a previous study.<sup>20</sup>

### 3. Results and discussion

The bare  $\text{BiVO}_4$  film photoanode was fabricated according to a previously employed procedure,<sup>6</sup> while the  $\text{NiFeV}$  LDH nanoparticles were synthesized by a typical one-pot hydrothermal method.<sup>46</sup> Then the preparation of  $\text{NiFeV/B-BiVO}_4$  was a simple two-step process. The borate pretreatment was performed according to our previous report.<sup>35</sup> Subsequently, a diluted suspension of  $\text{NiFeV}$  LDH was drop-casted onto the surface of the  $\text{B-BiVO}_4$  electrode, instead of the *in situ* hydrothermal/solvothermal growth<sup>30,50–52</sup> and electrodeposition.<sup>53–55</sup> In the two abovementioned methods, LDHs either grow homogeneously *in situ* and completely cover the surface of  $\text{BiVO}_4$  as oriented nanosheets or form a layer wrapped around the  $\text{BiVO}_4$  particles. However,  $\text{BiVO}_4$  is sensitive to the pH of the electroplating solution and the applied potential during electrolysis,<sup>56–58</sup> and the relatively high temperature of the hydrothermal process might cause detrimental surface etching on  $\text{BiVO}_4$ .<sup>59</sup> Considering the instability of borate treated  $\text{BiVO}_4$ ,<sup>35</sup> it is clearly challenging to maintain the pre-enhanced PEC activity of  $\text{B-BiVO}_4$  when loading OECs. In this case, drop-casting of OEC co-catalysts was expected to keep the  $\text{B-BiVO}_4$  electrode surface intact to the maximum extent. Prior to physical characterization and PEC testing, the mass loading of  $\text{NiFeV}$  LDH was optimized to  $10 \mu\text{g cm}^{-2}$  using bare  $\text{BiVO}_4$  as the substrate (Fig. S1, ESI†). Hence, all LDH/ $\text{BiVO}_4$ -based photoanodes were prepared with the same mass loading of  $10 \mu\text{g cm}^{-2}$  for the subsequent experiments.

The UV/Vis absorption spectrum of  $\text{B-BiVO}_4$  (Fig. S2, ESI†) was almost unchanged after  $\text{NiFeV}$  LDH loading, indicating that the band gaps of  $\text{B-BiVO}_4$  and  $\text{NiFeV/B-BiVO}_4$  were the same (2.54 eV). The X-ray diffraction (XRD) patterns of the  $\text{NiFeV}$  LDH,  $\text{B-BiVO}_4$  and  $\text{NiFeV/B-BiVO}_4$  electrodes are shown in Fig. S3 (ESI†). Apart from the FTO signals, all XRD peaks can be attributed to monoclinic  $\text{BiVO}_4$ . After drop-casting of  $\text{NiFeV}$  LDH on the  $\text{B-BiVO}_4$  electrode, a discernable reflection peak at  $2\theta = 11.4^\circ$  can be observed in the pattern of  $\text{NiFeV/B-BiVO}_4$  compared to that of bare  $\text{BiVO}_4$ , which could be attributed to the (003) lattice plane of  $\text{NiFeV}$ .<sup>40–42</sup> However, the additional main diffraction peaks of  $\text{NiFeV}$  LDH were too weak to identify due to the very low loading amount on the surface of  $\text{B-BiVO}_4$ .<sup>60,61</sup>

The morphologies of the  $\text{NiFeV}$  LDHs were first studied by transmission electron microscopy (TEM).  $\text{NiFeV}$  LDHs display rippled nanosheets with a size of several hundred nanometers and a thickness of  $\sim 3\text{--}5$  nm, which is in accordance with

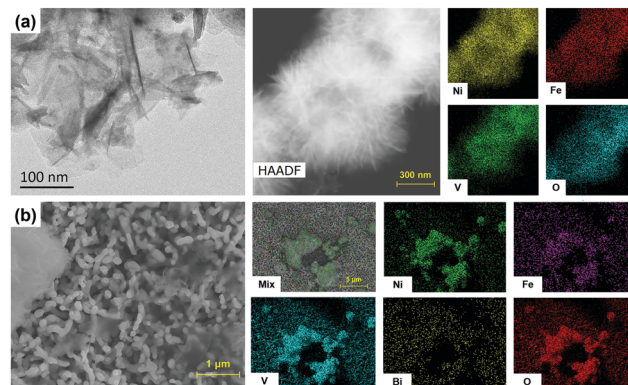


Fig. 1 (a) The TEM image and high-angle annular dark-field scanning TEM (HAADF-STEM) image of  $\text{NiFeV}$  nanosheets with the corresponding elemental mapping images. (b) The top-view SEM image of  $\text{NiFeV/B-BiVO}_4$  and the corresponding elemental mapping images.

previous reports in spite of the small differences in the ratio of each metal element.<sup>40–42</sup> The aggregates with laminations were observed by field emission scanning electron microscopy (FE-SEM), and the atomic ratios of Ni, Fe, and V were determined by EDX analysis (Fig. S4, ESI†), showing that the Ni : Fe : V molar ratio (2.83 : 0.22 : 1) was close to the ratio of the starting materials (3 : 0.2 : 1). The SEM images in Fig. 1b demonstrated that the  $\text{NiFeV}$  nanosheets were distributed over the surface of  $\text{BiVO}_4$  with aggregate phases (which occurred during the drying stage of drop-casting), which was also confirmed by the corresponding elemental mapping images. Drop-casting of  $\text{NiFeV}$  LDH on  $\text{BiVO}_4$  did not alter the quintessential worm-like morphology of the latter, which was characterized by a dendritic diameter of 300–400 nm and an average thickness of about  $\sim 650$  nm (Fig. S5, ESI†).

The X-ray photoelectron spectroscopy (XPS) measurement was carried out to examine the elemental composition of the  $\text{NiFeV/B-BiVO}_4$  surface by taking the C 1s peak at 284.8 eV as a standard reference (Fig. 2a). As expected, the noticeable Ni (Fig. 2b) and Fe signals (Fig. 2c) in the XPS spectra derived from LDHs (Fig. S6, ESI†) and a mixed V environment composed of  $\text{NiFeV}$  and  $\text{BiVO}_4$  were observed in the V 2p spectrum of Fig. 2d. As can be seen from Fig. 2e, the binding energies of 158.9 eV and 164.2 eV can be ascribed to  $\text{Bi } 4f_{7/2}$  and  $\text{Bi } 4f_{5/2}$ ,<sup>27</sup> respectively. For the O 1s core-level spectra (Fig. 2f), two peaks can be clearly identified.<sup>47,62</sup> In particular, the peak at 529.8 eV belongs to lattice oxygen, clearly originating from  $\text{BiVO}_4$ . While the O 1s peak at 531.7 eV is associated with surface hydroxy species, in our case, it was closely related to both the chemisorption of  $[\text{B}(\text{OH})_4]^-$  upon borate treatment<sup>35,63</sup> and  $\text{NiFeV}$  modification (Fig. S6, ESI†). Although no obvious B 1s signals were detected,<sup>35</sup> overall the XPS spectra indicated that  $\text{NiFeV}$  LDHs were successfully loaded onto the surface of the  $\text{B-BiVO}_4$  photoanode.

The PEC water oxidation activities of  $\text{NiFeV/B-BiVO}_4$  and other relevant photoanodes were measured in 1.0 M potassium borate buffer solution at pH 9.3 under AM 1.5 G simulated illumination. As shown in Fig. 3a, the photocurrent density of



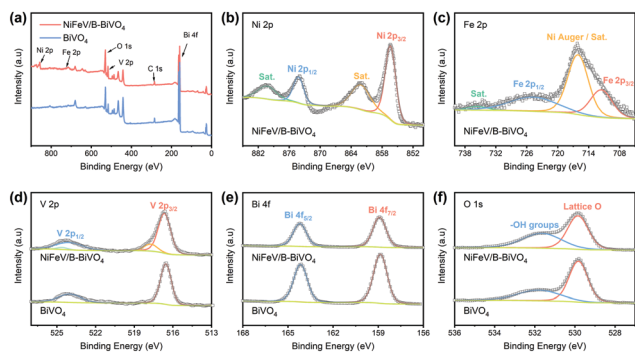


Fig. 2 (a) XPS survey spectra of bare  $\text{BiVO}_4$  and  $\text{NiFeV/B-BiVO}_4$  photoanodes and the high-resolution spectra of the corresponding (b) Ni 2p, (c) Fe 2p, (d) V 2p, (e) Bi 4f, and (f) O 1s. The dotted lines (squares) represent raw data and color lines indicate individual peak-fitting results.

bare  $\text{BiVO}_4$  at  $1.23 V_{\text{RHE}}$  was about  $1.6 \text{ mA cm}^{-2}$ .  $\text{NiFeV/BiVO}_4$  and  $\text{NiFeV/B-BiVO}_4$  showed much earlier photocurrent onsets (defined at  $0.1 \text{ mA cm}^{-2}$  photocurrent density) of  $0.22 V_{\text{RHE}}$  and  $0.21 V_{\text{RHE}}$ , respectively, and generated higher photocurrent in the low bias region ( $E < 0.6 V_{\text{RHE}}$ ), which is also corroborated by the dark current density results (Fig. S7, ESI†). In the high bias region ( $E > 0.9 V_{\text{RHE}}$ ), the PEC performance of  $\text{B-BiVO}_4$  was parallel to that of  $\text{NiFeV/BiVO}_4$ . After the borate and  $\text{NiFeV}$  LDH co-modification, the photocurrent density of  $\text{NiFeV/B-BiVO}_4$  reached  $4.6 \text{ mA cm}^{-2}$ , significantly outperforming either of the singly modified photoanodes ( $\sim 3.5 \text{ mA cm}^{-2}$ ). Such a synergistic effect was also observed in the applied bias photon-to-current efficiency (ABPE) and incident photon-to-current conversion efficiency (IPCE) measurements (Fig. 3b and c). The maximum ABPE of  $\text{NiFeV/B-BiVO}_4$  was 1.85% at  $0.62 V_{\text{RHE}}$ , which is

8 times as high as that of unmodified  $\text{BiVO}_4$  (0.23% at  $0.91 V_{\text{RHE}}$ ), and the IPCE of  $\text{NiFeV/B-BiVO}_4$  reached a maximum of  $\sim 80\%$  at  $1.23 V_{\text{RHE}}$  at a wavelength of  $\sim 380 \text{ nm}$ . It is important to note here that the photocurrent increase in the low bias region for  $\text{NiFeV/B-BiVO}_4$  goes beyond the simple accumulation of effects from  $\text{NiFeV}$  LDH and borate species, displaying a truly synergistic behavior (Fig. 3a and b) and indicating the positive cooperation between two co-modifications. Compared with previously reported  $\text{BiVO}_4$  photoanodes modified with the LDH co-catalyst, the PEC performance of  $\text{NiFeV/B-BiVO}_4$  is ranked among the best (Table S1, ESI†). For example, Wang and co-workers deposited a ternary  $\text{NiFeY}$  LDH on  $\text{BiVO}_4$  and the resulting photoanode exhibited remarkable PEC performance ( $\sim 5.2 \text{ mA cm}^{-2}$  at  $1.23 V_{\text{RHE}}$ ) with outstanding stability at  $0.8 V_{\text{RHE}}$  over 25 h,<sup>64</sup> while its onset potential ( $0.31 V_{\text{RHE}}$ ) remained reasonably high. The  $\text{CoPO}_3/\text{pGO}/\text{LDH}/\text{BiVO}_4$  composite photoanode,<sup>30</sup> reported by Li and co-workers, had an unprecedentedly low onset potential (0.17 V) and a high photocurrent ( $4.45 \text{ mA cm}^{-2}$ ); however, it required laborious multi-step procedures to obtain an integrated photoanode using four components.

Under chopped light illumination (Fig. 3d), the unmodified  $\text{BiVO}_4$  showed large photocurrent transient spikes for each light on-off cycle. On the contrary, these transient spikes were eliminated to a large extent in the  $\text{NiFeV/B-BiVO}_4$  photoanode, implying that the severe surface recombination on  $\text{BiVO}_4$  was significantly decreased after borate and  $\text{NiFeV}$  co-modification. Theoretically, the measured photocurrent density ( $J_{\text{PEC}}$ ) is governed by the relation:  $J_{\text{PEC}} = J_{\text{abs}} \times \eta_{\text{bulk}} \times \eta_{\text{surface}}$ ,<sup>6,32</sup> where  $J_{\text{abs}}$  is the photon absorption rate expressed as the current density at 100% internal quantum efficiency,  $\eta_{\text{bulk}}$  refers to the

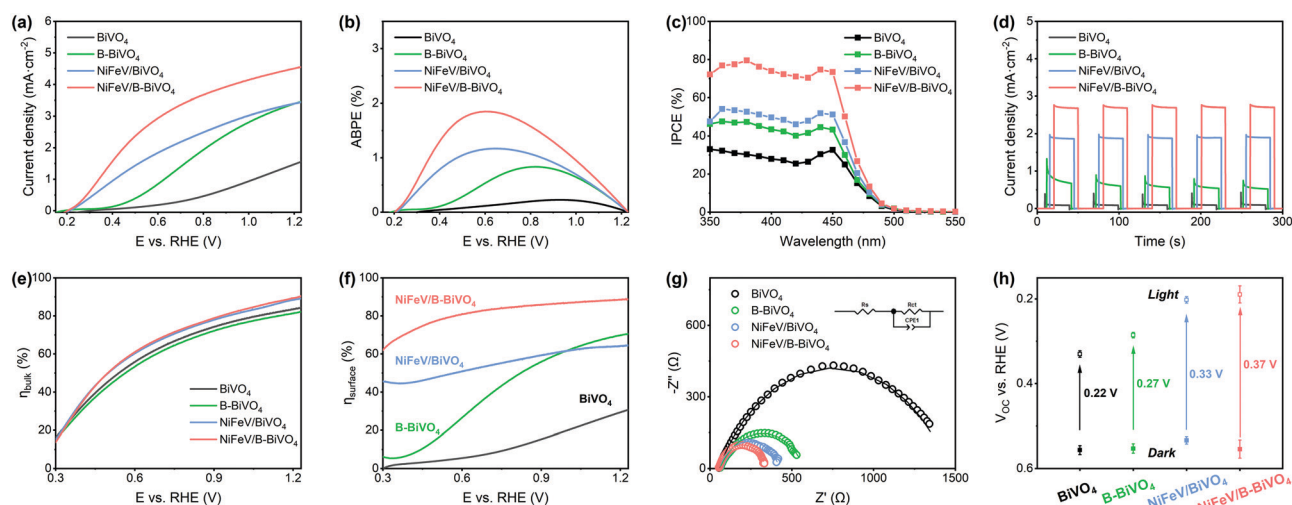


Fig. 3 (a) Linear sweep voltammetry (LSV) curves of  $\text{BiVO}_4$ ,  $\text{B-BiVO}_4$ ,  $\text{NiFeV/BiVO}_4$ , and  $\text{NiFeV/B-BiVO}_4$  photoanodes under AM 1.5G illumination in a 1.0 M potassium borate buffer at pH 9.3 (scan rate:  $10 \text{ mV s}^{-1}$ ). (b) ABPE curves of photoanodes calculated from LSV curves. (c) IPCEs of photoanodes at  $1.23 V_{\text{RHE}}$ . (d) Transient photocurrent curves under chopped illumination at a constant bias of  $0.6 V_{\text{RHE}}$ . (e) Charge separation efficiencies ( $\eta_{\text{bulk}}$ ) in the bulk of photoanodes estimated by comparing the photocurrent density of sulfite oxidation and the maximum theoretical photocurrent density from light absorption (according to the AM 1.5G solar spectrum and UV-vis absorbance). (f) Surface charge transfer efficiencies ( $\eta_{\text{surface}}$ ) of photoanodes obtained from the LSV curves of water oxidation and sulfite oxidation. (g) EIS curves of  $\text{BiVO}_4$ ,  $\text{NiFeV/BiVO}_4$ , and  $\text{NiFeV/B-BiVO}_4$  photoanodes under AM 1.5G illumination in 1.0 M potassium borate buffer at pH 9.3. (h) Open-circuit voltages ( $V_{\text{oc}}$ ) of photoanodes in the dark (solid) and under AM 1.5G simulated illumination (hollow).



yield of the photogenerated holes that reach the electrode/electrolyte interface, and  $\eta_{\text{surface}}$  indicates the charge injection efficiency of surface-reaching holes into the electrolyte for water oxidation. To gain an in-depth understanding of synergistic effects on carrier kinetics,  $\eta_{\text{bulk}}$  and  $\eta_{\text{surface}}$  of  $\text{BiVO}_4$  photoanodes were investigated carefully. As can be seen from Fig. 3e, the  $\eta_{\text{bulk}}$  values of all photoanodes were over 80% at 1.23  $V_{\text{RHE}}$ , benefiting from the well-established synthesis method of  $\text{BiVO}_4$  by Choi and co-workers.<sup>6</sup> There was almost no difference in  $\eta_{\text{bulk}}$  between  $\text{BiVO}_4$  and B- $\text{BiVO}_4$ , whereas the  $\eta_{\text{bulk}}$  of  $\text{BiVO}_4$  was somewhat improved after loading with NiFeV LDHs. This small increment of  $\eta_{\text{bulk}}$ , however, was not expected to contribute much to the remarkable activity of the NiFeV/B- $\text{BiVO}_4$  photoanode. Additionally, the Mott-Schottky (MS) plots (Fig. S8, ESI†) showed that, at each frequency, the slopes of both B- $\text{BiVO}_4$  and NiFeV/ $\text{BiVO}_4$  were marginally lower than that of bare  $\text{BiVO}_4$ , suggesting that the donor density of  $\text{BiVO}_4$  just slightly increased. Overall, these results fully indicated that both borate and NiFeV modifications had little effect on bulk properties within the  $\text{BiVO}_4$  electrode. By comparing the photocurrent densities of photoanodes with and without  $\text{Na}_2\text{SO}_3$  as a hole scavenger (Fig. 3f and Fig. S9, ESI†), a superior  $\eta_{\text{surface}}$  of NiFeV/B- $\text{BiVO}_4$  was about 90% at 1.23  $V_{\text{RHE}}$ , which was 3 times higher than that of bare  $\text{BiVO}_4$  (31%). In particular, it is worth noting that the  $\eta_{\text{surface}}$  of NiFeV/ $\text{BiVO}_4$  was much better than that of B- $\text{BiVO}_4$  at a lower applied bias; when the bias was further increased to  $>1.0$   $V_{\text{RHE}}$ , the  $\eta_{\text{surface}}$  of B- $\text{BiVO}_4$  became comparable to that of NiFeV/ $\text{BiVO}_4$ . The trends of the  $\eta_{\text{surface}}$  were consistent with their PEC performances (Fig. 3a) and evinced that both borate and LDH modifications were efficient in accelerating the surface charge carrier kinetics for OER.

The interfacial carrier kinetics was further investigated by using electrochemical impedance spectroscopy (EIS). As can be seen from Fig. 3g, the semicircles of Nyquist plots for all photoanodes fitted well with an equivalent circuit model (inset in Fig. 3g) composed of a series resistance ( $R_s$ ), an interfacial charge transfer resistance ( $R_{\text{ct}}$ ) and a constant phase angle element (CPE).<sup>20,65,66</sup> All modified photoanodes featured noticeably smaller semicircles in EIS plots compared to bare  $\text{BiVO}_4$ . In particular, the  $R_{\text{ct}}$  value of NiFeV/B- $\text{BiVO}_4$  was only 289.2  $\Omega$  (Table S2, ESI†) at 0.6  $V_{\text{RHE}}$ , implying the fastest charge transfer at the electrode/electrolyte interface by borate and NiFeV co-modification, which was demonstrated in the trends of  $\eta_{\text{surface}}$  as shown in Fig. 3f. The band bending was further investigated by open-circuit voltage ( $V_{\text{oc}}$ ) measurements. The photovoltage of a photoanode arises from the splitting of the electron and hole quasi-Fermi level under steady-state light illumination, which acts as a driving force for injecting the photogenerated holes into the electrolyte for OER.<sup>65,67</sup> According to several previous studies,<sup>30,43,49,62,68</sup> the simple integration of OECs on the surface of photoanodes could enlarge the difference in photovoltage between the dark and light conditions, resulting in greater band bending.<sup>44</sup> Smith and co-workers also reported that the photocharged  $\text{BiVO}_4$  photoanodes in a borate buffer solution achieved favorable band bending, which is responsible for the strong suppression of surface recombination.<sup>37</sup> From Fig. 3h, the photovoltages of  $\text{BiVO}_4$ ,

B- $\text{BiVO}_4$ , NiFeV/ $\text{BiVO}_4$ , and NiFeV/B- $\text{BiVO}_4$  were 0.22 V, 0.27 V, 0.33 V and 0.37 V, respectively. After NiFeV and borate co-modification, a greater driving force for water oxidation with more efficient charge separation in the photoanode was obtained, which resulted in a more negative onset potential for OER.<sup>30</sup>

It has been reported that both reduced charge surface recombination and enhanced water oxidation kinetics could contribute to the improvement of surface charge transfer efficiency.<sup>69–72</sup> In order to understand the main reason for the synergistically enhanced PEC performance, intensity modulated photocurrent spectroscopy (IMPS) was performed in the low bias region (0.3–0.6  $V_{\text{RHE}}$ ) to measure charge transfer rate constant ( $k_{\text{trans}}$ ) and surface recombination rate constant ( $k_{\text{rec}}$ ), respectively.<sup>47,73,74</sup> According to the generalized theory of IMPS, as the frequency increases, the relaxation in the concentration of photogenerated holes at the semiconductor surface is characterized by  $f_{\text{max}}$  (at the apex of the upper semicircle), where  $2\pi f_{\text{max}} = k_{\text{trans}} + k_{\text{rec}}$ .<sup>75,76</sup> The charge transfer efficiency, in terms of  $k_{\text{trans}}/(k_{\text{trans}} + k_{\text{rec}})$ , can be derived from the intersections of the semicircle with the real axis at low and high frequencies (*i.e.*,  $I_1$  and  $I_2$ , respectively), where  $I_1/I_2 = k_{\text{trans}}/(k_{\text{trans}} + k_{\text{rec}})$ .

Therefore, the absolute values of the phenomenological rate constants  $k_{\text{trans}}$  and  $k_{\text{rec}}$  were readily obtained. Typical IMPS responses of bare  $\text{BiVO}_4$  and NiFeV/B- $\text{BiVO}_4$  are shown in Fig. 4a and b, respectively. The upper semicircle of  $\text{BiVO}_4$  did not change noticeably upon the increase of applied bias, implying the severe charge recombination existing on bare  $\text{BiVO}_4$ ,<sup>54,77</sup> conversely, the upper semicircle of the NiFeV/B- $\text{BiVO}_4$  photoanode became smaller when the applied bias was increased. The  $k_{\text{rec}}$  of bare  $\text{BiVO}_4$  did not change significantly over the entire potential range (Fig. 4c). In sharp contrast, significantly lower  $k_{\text{rec}}$  values were observed for NiFeV/B- $\text{BiVO}_4$ . Even at the lowest applied bias of 0.3  $V_{\text{RHE}}$ , the  $k_{\text{rec}}$  of bare  $\text{BiVO}_4$  was up to 15.9  $\text{s}^{-1}$ , which was larger than that of NiFeV/B- $\text{BiVO}_4$  (4.6  $\text{s}^{-1}$ ) by a factor of 3.5. Most notably, at the point of maximum ABPE value of NiFeV/B- $\text{BiVO}_4$  (*i.e.*, 0.6  $V_{\text{RHE}}$ ), this ratio approached a value of 90, indicating that

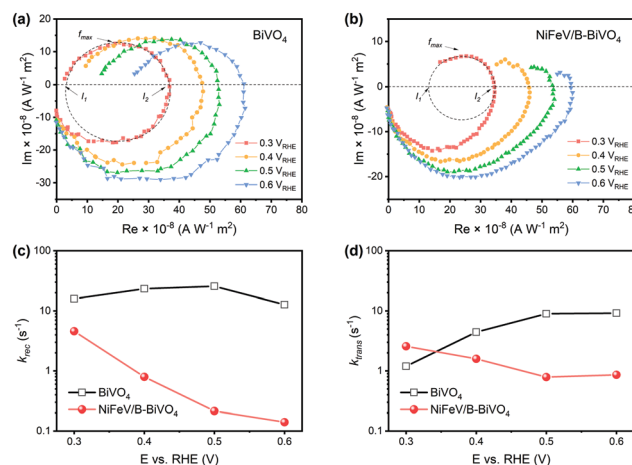


Fig. 4 IMPS responses of (a)  $\text{BiVO}_4$  and (b) NiFeV/B- $\text{BiVO}_4$  photoanodes at various potentials. (c) The rate constant for charge recombination ( $k_{\text{rec}}$ ) and (d) the rate constant for charge transfer ( $k_{\text{trans}}$ ) extracted from the IMPS spectra.





the charge recombination was greatly suppressed over the entire potential range. These results coincided with the enhancement (*inter alia*  $E < 0.6 V_{\text{RHE}}$ ) of photocurrent density of NiFeV/B-BiVO<sub>4</sub> (Fig. 3a) and further confirmed the dominating role of NiFeV co-catalysts within the synergy.

Generally, loading an OEC catalyst on a photoanode should result in an increase in water oxidation rates.<sup>16,20,43</sup> However, the  $k_{\text{trans}}$  value of bare BiVO<sub>4</sub> appeared to be higher than that of NiFeV/B-BiVO<sub>4</sub> to some extent at most potentials (Fig. 4d). This abnormal phenomenon has also been analogously observed in CoPi/BiVO<sub>4</sub>,<sup>70</sup> NiFeO<sub>x</sub>/Fe<sub>2</sub>O<sub>3</sub>,<sup>78</sup> Co-LaFeO<sub>3</sub>/BiVO<sub>4</sub>,<sup>16</sup> and so on. It should be noted that the smaller  $k_{\text{trans}}$  measured here on NiFeV/B-BiVO<sub>4</sub> does not certainly suggest slower water oxidation. This is because the  $k_{\text{trans}}$  derived from IMPS more likely corresponds to the rate-determining steps (RDS) of the complex charge transfer processes from the photoelectrode to water.<sup>78</sup> Moreover, NiFeV LDH has been confirmed as an efficient water oxidation catalyst according to our electrochemical testing (Fig. S10, ESI†) and related literature.<sup>40–42</sup> Furthermore, the actual charge transfer efficiency  $k_{\text{trans}}/(k_{\text{trans}} + k_{\text{rec}})$  of NiFeV/B-BiVO<sub>4</sub> was evidently higher than that of bare BiVO<sub>4</sub> (Fig. S11, ESI†) owing to minimized recombination, displaying the same trend as the  $\eta_{\text{surface}}$  results in Fig. 3f. To further support this experimentally, the H/D kinetic isotope effect (KIE) was assessed by comparing photocurrent densities at different overpotentials (after corrections) in 0.1 M anhydrous borax (Na<sub>2</sub>B<sub>4</sub>O<sub>7</sub>) H<sub>2</sub>O and D<sub>2</sub>O solutions (Fig. S12, ESI†).<sup>20</sup> Herein, H/D KIE studies were performed to investigate the proton transfer kinetics and probe the RDS in the water oxidation process on the surface of BiVO<sub>4</sub>.<sup>79,80</sup> The KIE of the bare BiVO<sub>4</sub> photoanode approached 1.5, in agreement with a previous report,<sup>20</sup> indicating that the RDS of PEC water oxidation on BiVO<sub>4</sub> involved the proton transfer process. B-BiVO<sub>4</sub> showed a moderate KIE value of  $\sim 1.2$ , which indicated slight acceleration of proton transfer. After loading LDH co-catalysts, both

NiFeV/BiVO<sub>4</sub> and NiFeV/B-BiVO<sub>4</sub> displayed negligible H/D kinetic isotope effects (KIE  $\approx 1.0$ ) at all applied potentials, suggesting that the proton transfer is no longer involved in the RDS.<sup>80</sup> Moreover, it revealed that hole transfer into the LDH co-catalysts (instead of catalytic processes of water oxidation on the BiVO<sub>4</sub> surface) is rate-limiting,<sup>79</sup> indicative of very fast subsequent injection of photogenerated holes into the electrolyte. It might be therefore concluded that the synergistic effects of borate and NiFeV co-modifications not only increased the overall rate of water oxidation, but also promoted charge transfer and reduced charge recombination.

In our previous report,<sup>35</sup> the adsorption of borate on the surface of BiVO<sub>4</sub> resulted in a molecular level modification, which reduced surface charge trapping, thereby causing a significant increase in the photocurrent of B-BiVO<sub>4</sub>. However, this improvement gradually degenerated within short-term photolysis (Fig. 5a and Fig. S13, ESI†). The degradation of efficiency was likely caused by the accumulation of photogenerated holes at the B-BiVO<sub>4</sub> surface, where they easily recombined with electrons and could not be consumed for water oxidation quickly.<sup>29,72,81</sup> When using the electrolyte with the Na<sub>2</sub>SO<sub>3</sub> hole scavenger (Fig. 5b), the photocurrent of B-BiVO<sub>4</sub> was maintained after 1 h photolysis at 0.6 V<sub>RHE</sub> in that electrolyte. After NiFeV LDH modification, as shown in Fig. 5c, the NiFeV/B-BiVO<sub>4</sub> photoanode exhibited good stability and about 95% of the initial photocurrent density was retained after 8 h photolysis. A long-term stability test (24 h at 0.6 V<sub>RHE</sub>) of NiFeV/B-BiVO<sub>4</sub> showed that over 80% of the initial photocurrent density was maintained (Fig. S14, ESI†). Besides, a high faradaic efficiency of 95% was obtained for NiFeV/B-BiVO<sub>4</sub> (Fig. S15, ESI†); both the morphology of BiVO<sub>4</sub> and the nanostructures of the catalysts did not show obvious changes after stability tests (Fig. S16, ESI†). The improvement of photostability could be attributed to the improved interfacial charge transfer efficiency by the NiFeV catalyst, which can reduce surface

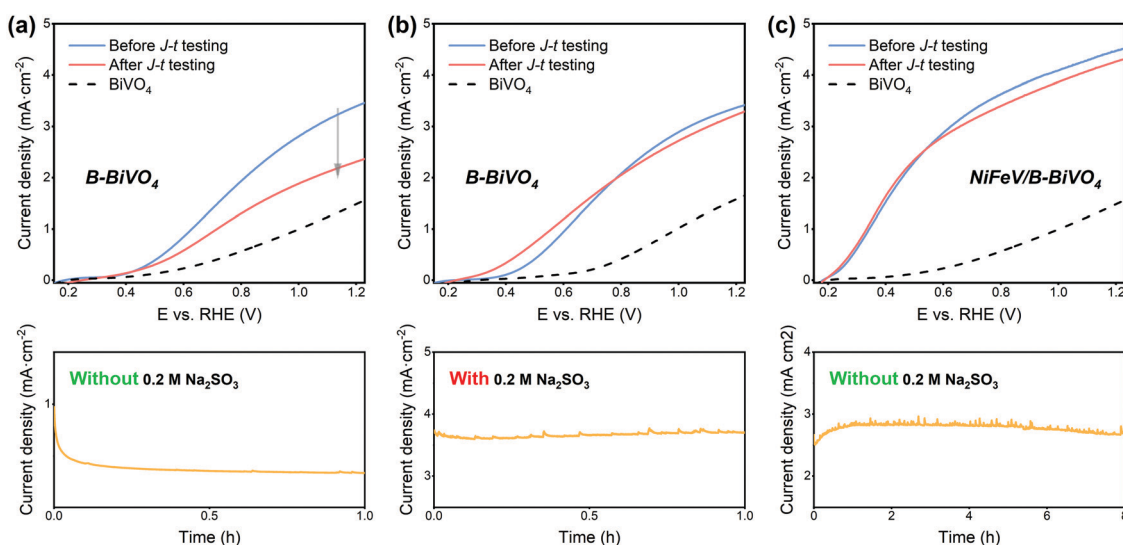
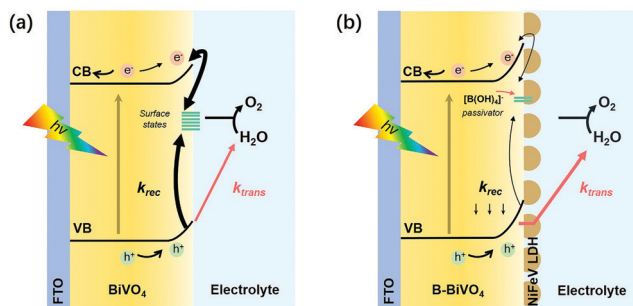


Fig. 5 LSV curves of B-BiVO<sub>4</sub> before and after  $J$ - $t$  testing in 1.0 M potassium borate buffer (pH 9.3) (a) without and (b) with 0.2 M Na<sub>2</sub>SO<sub>3</sub> at 0.6 V<sub>RHE</sub> for 1 h, and the bottom figures show the corresponding  $J$ - $t$  curves; (c) LSV curves of NiFeV/B-BiVO<sub>4</sub> before and after  $J$ - $t$  testing in 1.0 M potassium borate buffer (pH 9.3) at 0.6 V<sub>RHE</sub> and the corresponding  $J$ - $t$  curves.





Scheme 1 Schematic illustration of the working principles of (a) bare  $\text{BiVO}_4$  and (b)  $\text{NiFeV/B-BiVO}_4$  photoanodes.

recombination and kinetically suppress photocorrosion.<sup>29,36,82,83</sup> Besides, it has been reported that the injection of surface-reaching holes into OECs was thermodynamically favorable compared to direct transfer to the solution and the catalysts were typically permeable for the electrolyte and redox-active.<sup>44</sup> Therefore, holes can accumulate throughout the LDHs, thereby diminishing surface recombination.<sup>30</sup>

These results clearly demonstrated that loading LDH co-catalysts onto  $\text{B-BiVO}_4$  did not only further enhance the photocurrent density and lower the onset potential, but also significantly improved the stability of  $\text{B-BiVO}_4$ . This synergetic effect of borate treatment and LDH modification can also be realized on  $\text{NiFeV/B-BiVO}_4$  (Fig. S17, ESI<sup>†</sup>) and  $\text{NiV/B-BiVO}_4$  photoanodes (Fig. S18, ESI<sup>†</sup>), which can achieve photocurrents of  $\sim 3.7 \text{ mA cm}^{-2}$  and  $\sim 4.3 \text{ mA cm}^{-2}$  at  $1.23 \text{ V}_{\text{RHE}}$ , respectively, with relatively low onset potentials ( $\sim 0.25 \text{ V}_{\text{RHE}}$ ) and good stability.

From the above discussions, the overall effects of charge transfer and surface recombination are schematically summarized in Scheme 1. For bare  $\text{BiVO}_4$ , the photogenerated holes can be directly consumed for water oxidation or trapped by surface state and recombined with electrons. The co-modification showed slight improvement in the intrinsically decent charge separation of bare  $\text{BiVO}_4$ . The self-anchored borate species serve as a passivator contributing to the decrease of surface charge recombination as well as a ligand in modifying the catalytic site for water oxidation.<sup>35,36</sup> Furthermore, the main role of  $\text{NiFeV LDH}$  is to efficiently suppress surface recombination and promote interfacial charge transfer efficiency, thereby improving PEC performance and stability simultaneously. The high intrinsic catalytic activity of  $\text{NiFeV LDH}$  is also conducive to a greater driving force for water oxidation and a lower onset potential.

## 4. Conclusions

In conclusion, our work provided insights into the rational design of a  $\text{BiVO}_4$  based photoanode for highly efficient PEC water splitting combined with post-synthetic borate treatment and  $\text{NiFeV}$  co-catalyst loading. The optimized  $\text{NiFeV/B-BiVO}_4$  photoanode achieved a remarkable photocurrent density of  $4.6 \text{ mA cm}^{-2}$  with an ultra-low onset potential ( $0.2 \text{ V}_{\text{RHE}}$ ) with a high ABPE of 1.85% at  $0.6 \text{ V}_{\text{RHE}}$ . It is worth noting that  $\text{NiFeV/B-BiVO}_4$  exhibited a strong photocurrent increase over a low

applied bias range ( $< 0.6 \text{ V}_{\text{RHE}}$ ). More importantly, studies on  $\text{NiFeV/B-BiVO}_4$  surface kinetics further demonstrated the outstanding contribution of  $\text{NiFeV}$  co-modification to the suppression of charge recombination and the promotion of charge transfer efficiency. Moreover, loading with the  $\text{NiFeV}$  co-catalyst significantly improves the stability of borate-treated  $\text{BiVO}_4$ . This work has revealed and emphasized the significance of the synergy of co-modifications in photoelectrochemical devices.

## Conflicts of interest

There are no conflicts to declare.

## Acknowledgements

This work was financially supported by the Swedish Research Council (2017-00935), Knut and Alice Wallenberg Foundation (KAW 2016.0072), and the Foundation of Westlake University. The authors thank the Instrumentation and Service Center for Physical Sciences (ISCPS) at Westlake University (Hangzhou, China) for the assistance in measurement and data interpretation. Q. Meng is thankful to the China Scholarship Council for a special scholarship award.

## References

- 1 M. Grätzel, *Nature*, 2001, **414**, 338–344.
- 2 J. H. Kim, D. Hansora, P. Sharma, J.-W. Jang and J. S. Lee, *Chem. Soc. Rev.*, 2019, **48**, 1908–1971.
- 3 M. A. Lumley, A. Radmilovic, Y. J. Jang, A. E. Lindberg and K.-S. Choi, *J. Am. Chem. Soc.*, 2019, **141**, 18358–18369.
- 4 X. Ding, L. Zhang, Y. Wang, A. Liu and Y. Gao, *Coord. Chem. Rev.*, 2018, **357**, 130–143.
- 5 A. Kudo, K. Ueda, H. Kato and I. Mikami, *Catal. Lett.*, 1998, **53**, 229–230.
- 6 T. W. Kim and K.-S. Choi, *Science*, 2014, **343**, 990–994.
- 7 D. K. Lee, D. Lee, M. A. Lumley and K.-S. Choi, *Chem. Soc. Rev.*, 2019, **48**, 2126–2157.
- 8 J. Seo, H. Nishiyama, T. Yamada and K. Domen, *Angew. Chem., Int. Ed.*, 2018, **57**, 8396–8415.
- 9 Y. Park, K. J. McDonald and K.-S. Choi, *Chem. Soc. Rev.*, 2013, **42**, 2321–2337.
- 10 F. F. Abdi, T. J. Savenije, M. M. May, B. Dam and R. van de Krol, *J. Phys. Chem. Lett.*, 2013, **4**, 2752–2757.
- 11 H. S. Han, S. Shin, D. H. Kim, I. J. Park, J. S. Kim, P.-S. Huang, J.-K. Lee, I. S. Cho and X. Zheng, *Energy Environ. Sci.*, 2018, **11**, 1299–1306.
- 12 R. Li, F. Zhang, D. Wang, J. Yang, M. Li, J. Zhu, X. Zhou, H. Han and C. Li, *Nat. Commun.*, 2013, **4**, 1432.
- 13 S. Wang, G. Liu and L. Wang, *Chem. Rev.*, 2019, **119**, 5192–5247.
- 14 S. J. Hong, S. Lee, J. S. Jang and J. S. Lee, *Energy Environ. Sci.*, 2011, **4**, 1781–1787.
- 15 X. Chang, T. Wang, P. Zhang, J. Zhang, A. Li and J. Gong, *J. Am. Chem. Soc.*, 2015, **137**, 8356–8359.





- 16 Y. Gao, G. Yang, Y. Dai, X. Li, J. Gao, N. Li, P. Qiu and L. Ge, *ACS Appl. Mater. Interfaces*, 2020, **12**, 17364–17375.
- 17 W. J. Jo, J.-W. Jang, K.-j. Kong, H. J. Kang, J. Y. Kim, H. Jun, K. P. S. Parmar and J. S. Lee, *Angew. Chem., Int. Ed.*, 2012, **51**, 3147–3151.
- 18 J. M. Lee, J. H. Baek, T. M. Gill, X. Shi, S. Lee, I. S. Cho, H. S. Jung and X. Zheng, *J. Mater. Chem. A*, 2019, **7**, 9019–9024.
- 19 D. K. Zhong, S. Choi and D. R. Gamelin, *J. Am. Chem. Soc.*, 2011, **133**, 18370–18377.
- 20 F. Li, H. Yang, Q. Zhuo, D. Zhou, X. Wu, P. Zhang, Z. Yao and L. Sun, *Angew. Chem., Int. Ed.*, 2021, **60**, 1976–1985.
- 21 J.-B. Pan, B.-H. Wang, J.-B. Wang, H.-Z. Ding, W. Zhou, X. Liu, J.-R. Zhang, S. Shen, J.-K. Guo, L. Chen, C.-T. Au, L.-L. Jiang and S.-F. Yin, *Angew. Chem., Int. Ed.*, 2021, **60**, 1433–1440.
- 22 W. Yong, L. Fei, Z. Xu, Y. Fengshou, D. Jian, B. Lichen and S. Licheng, *Angew. Chem., Int. Ed.*, 2017, **56**, 6911–6915.
- 23 C. Xu, W. Sun, Y. Dong, C. Dong, Q. Hu, B. Ma and Y. Ding, *J. Mater. Chem. A*, 2020, **8**, 4062–4072.
- 24 X. Cao, C. Xu, X. Liang, J. Ma, M. Yue and Y. Ding, *Appl. Catal., B*, 2020, **260**, 118136.
- 25 B. Lamm, B. J. Trzeźniewski, H. Döschner, W. A. Smith and M. Stefiak, *ACS Energy Lett.*, 2017, **3**, 112–124.
- 26 B. Zhang, L. Chou and Y. Bi, *Appl. Catal., B*, 2020, **262**, 118267.
- 27 T. W. Kim, Y. Ping, G. A. Galli and K.-S. Choi, *Nat. Commun.*, 2015, **6**, 8769.
- 28 Q. Zhang, M. Liu, W. Zhou, Y. Zhang, W. Hao, Y. Kuang, H. Liu, D. Wang, L. Liu and J. Ye, *Nano Energy*, 2021, **81**, 105651.
- 29 J. A. Seabold and K.-S. Choi, *J. Am. Chem. Soc.*, 2012, **134**, 2186–2192.
- 30 S. Ye, C. Ding, R. Chen, F. Fan, P. Fu, H. Yin, X. Wang, Z. Wang, P. Du and C. Li, *J. Am. Chem. Soc.*, 2018, **140**, 3250–3256.
- 31 K.-H. Ye, H. Li, D. Huang, S. Xiao, W. Qiu, M. Li, Y. Hu, W. Mai, H. Ji and S. Yang, *Nat. Commun.*, 2019, **10**, 1–9.
- 32 J. H. Kim and J. S. Lee, *Adv. Mater.*, 2019, 1806938.
- 33 H. L. Tan, R. Amal and Y. H. Ng, *J. Mater. Chem. A*, 2017, **5**, 16498–16521.
- 34 D. Lee, W. Wang, C. Zhou, X. Tong, M. Liu, G. Galli and K.-S. Choi, *Nat. Energy*, 2021, **6**, 287–294.
- 35 Q. Meng, B. Zhang, L. Fan, H. Liu, M. Valvo, K. Edström, M. Cuartero, R. de Marco, G. A. Crespo and L. Sun, *Angew. Chem., Int. Ed.*, 2019, **58**, 19027–19033.
- 36 R.-T. Gao and L. Wang, *Angew. Chem., Int. Ed.*, 2020, **59**, 23094–23099.
- 37 N. J. Firet, A. Venugopal, M. A. Blommaert, C. Cavallari, C. J. Sahle, A. Longo and W. A. Smith, *Chem. Mater.*, 2019, **31**, 7453–7462.
- 38 B. J. Trzeźniewski, I. A. Digdaya, T. Nagaki, S. Ravishankar, I. Herraiz-Cardona, D. A. Vermaas, A. Longo, S. Gimenez and W. A. Smith, *Energy Environ. Sci.*, 2017, **10**, 1517–1529.
- 39 B. J. Trzeźniewski and W. A. Smith, *J. Mater. Chem. A*, 2016, **4**, 2919–2926.
- 40 K. N. Dinh, P. Zheng, Z. Dai, Y. Zhang, R. Dangol, Y. Zheng, B. Li, Y. Zong and Q. Yan, *Small*, 2018, **14**, 1703257.
- 41 J. Jiang, F. Sun, S. Zhou, W. Hu, H. Zhang, J. Dong, Z. Jiang, J. Zhao, J. Li, W. Yan and M. Wang, *Nat. Commun.*, 2018, **9**, 2885.
- 42 P. Li, X. Duan, Y. Kuang, Y. Li, G. Zhang, W. Liu and X. Sun, *Adv. Energy Mater.*, 2018, **8**, 1703341.
- 43 X. Ning, P. Du, Z. Han, J. Chen and X. Lu, *Angew. Chem., Int. Ed.*, 2021, **60**, 3504–3509.
- 44 F. A. Laskowski, M. R. Nellist, J. Qiu and S. W. Boettcher, *J. Am. Chem. Soc.*, 2018, **141**, 1394–1405.
- 45 B. Zhang, X. Huang, Y. Zhang, G. Lu, L. Chou and Y. Bi, *Angew. Chem., Int. Ed.*, 2020, **59**, 18990–18995.
- 46 K. Fan, H. Chen, Y. Ji, H. Huang, P. M. Claesson, Q. Daniel, B. Philippe, H. Rensmo, F. Li, Y. Luo and L. Sun, *Nat. Commun.*, 2016, **7**, 11981.
- 47 D. Zhou, K. Fan, Q. Zhuo, Y. Zhao and L. Sun, *ACS Appl. Mater. Interfaces*, 2021, **13**, 2723–2733.
- 48 K. Zhang, B. Jin, C. Park, Y. Cho, X. Song, X. Shi, S. Zhang, W. Kim, H. Zeng and J. H. Park, *Nat. Commun.*, 2019, **10**, 2001.
- 49 F. Tang, W. Cheng, H. Su, X. Zhao and Q. Liu, *ACS Appl. Mater. Interfaces*, 2018, **10**, 6228–6234.
- 50 Y. Tang, R. Wang, Y. Yang, D. Yan and X. Xiang, *ACS Appl. Mater. Interfaces*, 2016, **8**, 19446–19455.
- 51 W. He, R. Wang, L. Zhang, J. Zhu, X. Xiang and F. Li, *J. Mater. Chem. A*, 2015, **3**, 17977–17982.
- 52 L. Wang, F. Dionigi, N. T. Nguyen, R. Kirchgeorg, M. Gliech, S. Grigorescu, P. Strasser and P. Schmuki, *Chem. Mater.*, 2015, **27**, 2360–2366.
- 53 H. She, P. Yue, X. Ma, J. Huang, L. Wang and Q. Wang, *Appl. Catal., B*, 2020, **263**, 118280.
- 54 X. Lv, X. Xiao, M. Cao, Y. Bu, C. Wang, M. Wang and Y. Shen, *Appl. Surf. Sci.*, 2018, **439**, 1065–1071.
- 55 P. Yue, H. She, L. Zhang, B. Niu, R. Lian, J. Huang, L. Wang and Q. Wang, *Appl. Catal., B*, 2021, **286**, 119875.
- 56 H. Chen, S. Wang, J. Wu, X. Zhang, J. Zhang, M. Lyu, B. Luo, G. Qian and L. Wang, *J. Mater. Chem. A*, 2020, **8**, 13231–13240.
- 57 S. Wang, P. Chen, J. H. Yun, Y. Hu and L. Wang, *Angew. Chem., Int. Ed.*, 2017, **56**, 8500–8504.
- 58 D. Lee, A. Kvit and K.-S. Choi, *Chem. Mater.*, 2018, **30**, 4704–4712.
- 59 T. S. Sinclair, H. B. Gray and A. M. Müller, *Eur. J. Inorg. Chem.*, 2018, 1060–1067.
- 60 Y. He, C. Zhang, J. Hu and M. K. Leung, *Appl. Energy*, 2019, **255**, 113770.
- 61 Q. Wang, T. Niu, L. Wang, J. Huang and H. She, *Chinese J. Catal.*, 2018, **39**, 613–618.
- 62 S. Kumar and A. K. Satpati, *Electrochim. Acta*, 2020, 137565.
- 63 L. Shan, G.-l. Wang, J. Suriyaprakash, D. Li, L.-z. Liu and L.-m. Dong, *J. Alloys Compd.*, 2015, **636**, 131–137.
- 64 D. He, R.-T. Gao, S. Liu, M. Sun, X. Liu, K. Hu, Y. Su and L. Wang, *ACS Catal.*, 2020, **10**, 10570–10576.
- 65 S. Wang, T. He, P. Chen, A. Du, K. Ostrikov, W. Huang and L. Wang, *Adv. Mater.*, 2020, 2001385.
- 66 J. Jian, Y. Xu, X. Yang, W. Liu, M. Fu, H. Yu, F. Xu, F. Feng, L. Jia, D. Friedrich, R. van de Krol and H. Wang, *Nat. Commun.*, 2019, **10**, 2609.
- 67 M. R. Nellist, F. A. Laskowski, F. Lin, T. J. Mills and S. W. Boettcher, *Acc. Chem. Res.*, 2016, **49**, 733–740.
- 68 C. Du, X. Yang, M. T. Mayer, H. Hoyt, J. Xie, G. McMahon, G. Bischooping and D. Wang, *Angew. Chem., Int. Ed.*, 2013, **52**, 12692–12695.



- 69 D. R. Gamelin, *Nat. Chem.*, 2012, **4**, 965–967.
- 70 C. Zachäus, F. F. Abdi, L. M. Peter and R. van de Krol, *Chem. Sci.*, 2017, **8**, 3712–3719.
- 71 M. Barroso, C. A. Mesa, S. R. Pendlebury, A. J. Cowan, T. Hisatomi, K. Sivula, M. Grätzel, D. R. Klug and J. R. Durrant, *Proc. Natl. Acad. Sci. U. S. A.*, 2012, **109**, 15640–15645.
- 72 R. Liu, Z. Zheng, J. Spurgeon and X. Yang, *Energy Environ. Sci.*, 2014, **7**, 2504–2517.
- 73 F. Li, Y. Li, Q. Zhuo, D. Zhou, Y. Zhao, Z. Zhao, X. Wu, Y. Shan and L. Sun, *ACS Appl. Mater. Interfaces*, 2020, **12**, 11479–11488.
- 74 F. Yu, F. Li, T. Yao, J. Du, Y. Liang, Y. Wang, H. Han and L. Sun, *ACS Catal.*, 2017, **7**, 1868–1874.
- 75 R. Peat and L. Peter, *J. Electroanal. Chem.*, 1987, **228**, 351–364.
- 76 M. G. Ahmed, I. E. Kretschmer, T. A. Kandiel, A. Y. Ahmed, F. A. Rashwan and D. W. Bahnemann, *ACS Appl. Mater. Interfaces*, 2015, **7**, 24053–24062.
- 77 J. Xie, C. Guo, P. Yang, X. Wang, D. Liu and C. M. Li, *Nano Energy*, 2017, **31**, 28–36.
- 78 J. E. Thorne, J.-W. Jang, E. Y. Liu and D. Wang, *Chem. Sci.*, 2016, **7**, 3347–3354.
- 79 W. Li, D. He, S. W. Sheehan, Y. He, J. E. Thorne, X. Yao, G. W. Brudvig and D. Wang, *Energy Environ. Sci.*, 2016, **9**, 1794–1802.
- 80 Y. Zhang, H. Zhang, H. Ji, W. Ma, C. Chen and J. Zhao, *J. Am. Chem. Soc.*, 2016, **138**, 2705–2711.
- 81 F. M. Toma, J. K. Cooper, V. Kunzelmann, M. T. McDowell, J. Yu, D. M. Larson, N. J. Borys, C. Abelyan, J. W. Beeman, K. M. Yu, J. Yang, L. Chen, M. R. Shaner, J. Spurgeon, F. A. Houle, K. A. Persson and I. D. Sharp, *Nat. Commun.*, 2016, **7**, 12012.
- 82 D. K. Lee and K.-S. Choi, *Nat. Energy*, 2018, **3**, 53–60.
- 83 R.-T. Gao, D. He, L. Wu, K. Hu, X. Liu, Y. Su and L. Wang, *Angew. Chem., Int. Ed.*, 2020, **59**, 6213–6218.

